Mechanical Engineering

KAIST

2017 AGU Fall Meeting

Use of altimetry-derived sea surface heights for coastal surface submesoscale process studies

Jang Gon Yoo and Sung Yong Kim†

Department of Mechanical Engineering, Korea Advanced Institute of Science and Technology,
syongkim@kaist.ac.kr†

Abstract

This work evaluates feasibility and capability of the use of altimetry-derived data for coastal surface submesoscale process (hourly and km-scale) studies with comparisons among independent mesoscale and submesoscale observations including sea surface heights obtained from altimetry and tide gauges, and coastal radar-derived surface currents, and passive tracer maps obtained from geostationary ocean color imagery. The coastal surface currents are decomposed into current components associated with stream functions and velocity potentials, and their stream functions are comparable with mesoscale SSHs and contain finer scale features, i.e., submesoscale fronts and eddies, which are supported by Chlorophyll maps having hourly and 500-m resolution. Some of altimeter-derived and coastal-radar-derived data exhibit consistent mesoscale and submesoscale features and have a reasonable agreement with passive tracer maps as well.

Data

The study domain is chosen as a latitudinal band between 44°N and 45°N and from 130°W to the coast (a black box in Figure 1) in a coastal region of the northeast Pacific because (1) realistic simulations and ALT- and HFR-derived observations are available along the relatively simple coastline and (2) there is a clear separation of the inertial frequency from primary tides (K_1 and M_2), of which the corresponding clockwise inertial frequencies are -1.3893 cpd and -1.4142 cpd.

We analyze the SSHs and currents with hourly temporal and 2-km horizontal spatial resolutions for a period of approximately one year (August 2008 to August 2009) off the Oregon coast from forward numerical simulations forced by realistic wind stress and tides using the Regional Ocean Modeling System (ROMS) [see [1, 2] for more details]. The numerical model outputs using realistic boundary conditions and forces can simulate regional coastal circulations and variability in a manner that is dynamically and statistically consistent with observations and well capture the primary variability including low-frequency currents (e.g., coastal trapped waves), near-inertial currents, tidal currents [e.g., [1, 2]]. However, the numerical model outputs do not exactly duplicate the actual observations in time and space. Thus, we analyze the numerical model outputs in the delineation of geostrophy and ageostrophy and discuss their difference and potential limitations compared with observations later.

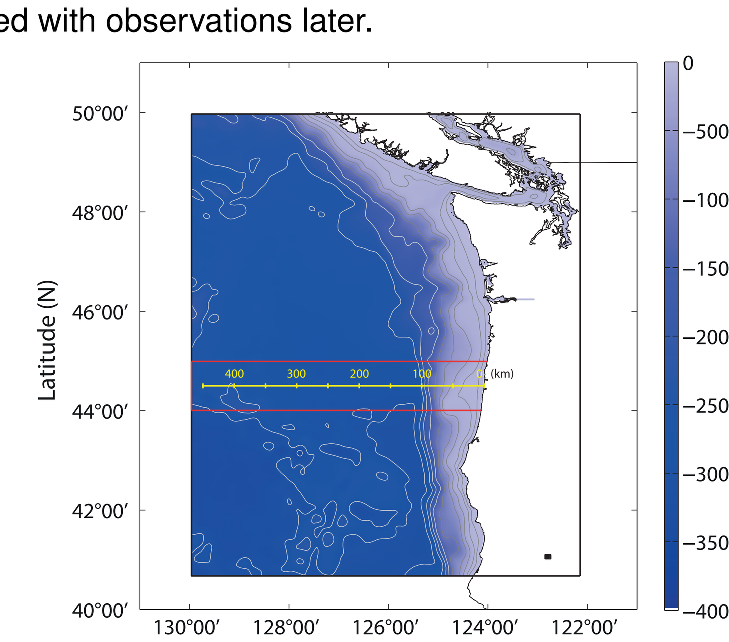

Figure 1: A study domain of submesoscale sea surface heights and coastal currents off the coast of Oregon. A latitudinal band between 44°N and 45°N is marked with red lines. Yellow tick marks denote a cross-shore distance from the shoreline (km). The bottom bathymetry is contoured at 50 m, 100 m, 250 m, 500 m, 1000 m, 1500 m, 2000 m, 2500 m, and 3000 m.

As the observational resources comparable to the numerical model outputs, we analyze the daily altimeter (ALT)-derived optimally interpolated (OI) AVISO geostrophic currents and SSHs, hourly HFR-derived surface radial velocity maps at resolutions of 1.5 km to 4 km and vector current maps at 6 km resolution off Oregon for a period of two years (2007 to 2008). In addition, the blended products of the ALT-derived SSHs (or anomalies) with the coastal tide gauge data using linear interpolation and inverse weighted interpolation are available for verification of the data.

Delineation of geostrophy and ageostrophy

We examine the currents and vorticity under both geostrophic and ageostrophic balances and identify the frequency bands which are valid for the geostrophic and ageostrophic balances. As an initial investigation, we focus on the variance distribution of the surface currents in the frequency domain as a function of distance from the coast.

Using the geostrophic balance, the SSHs (η) in the open ocean are converted into geostrophic currents [$\mathbf{u}_g = (u_g, v_g)$],

$$u_g(x,y) = -\frac{g}{f_c}\frac{\partial \eta(x,y)}{\partial y}, \qquad (1)$$

$$v_g(x,y) = \frac{g}{f_c}\frac{\partial \eta(x,y)}{\partial x}, \qquad (2)$$

where f_c and g denote the Coriolis frequency and gravitational acceleration, respectively. This geostrophic balance is known to be valid for mesoscale currents [e.g., [3]] and subdiurnal submesoscale currents [e.g., [4]] in the open ocean. In contrast, the currents [$\mathbf{u} = (u, v)$] in coastal regions may contain both geostrophic currents and ageostrophic currents [$\mathbf{u}_{ag} = (u_{ag}, v_{ag})$],

$$u_{ag}(x,y,z) = u(x,y,z) + \frac{g}{f_c}\frac{\partial \eta(x,y)}{\partial y}, \qquad (3)$$

$$v_{ag}(x,y,z) = v(x,y,z) - \frac{g}{f_c}\frac{\partial \eta(x,y)}{\partial x}. \qquad (4)$$

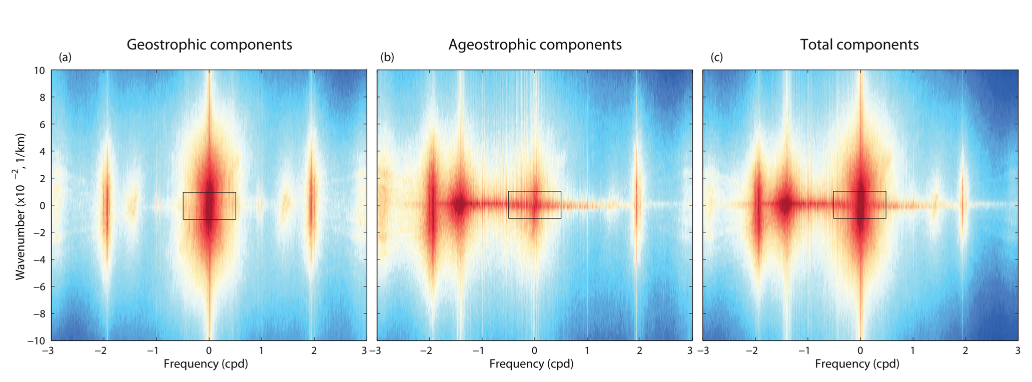

Figure 2: Energy spectra in the wavenumber and frequency domains ($\log_{10}$ scale, $\mathrm{cm}^2\,\mathrm{s}^{-2}\,\mathrm{km\,cpd}^{-1}$) of the ROMS-derived surface currents. (a) Geostrophic currents ($\mathbf{u}_g$). (b) Ageostrophic surface currents ($\mathbf{u}_{ag}$). (c) Total surface currents ($\mathbf{u} = \mathbf{u}_g + \mathbf{u}_{ag}$). Variance at non-zero frequency and non-zero wavenumber is shown. The temporal scale ($|\sigma| \le 0.5$ cpd; $T \ge 2$ days) and spatial scale ($|k| \le 0.01\ \mathrm{km}^{-1}$; $\lambda \ge 100$ km) of the oceanic mesoscale [e.g., [4]] are marked with black boxes.

The characteristics of the geostrophic currents and surface ageostrophic currents are examined with meridionally averaged energy spectra in the wavenumber and frequency domains (Figures 2a to 2c) of the hourly ROMS-derived geostrophic currents, ageostrophic surface currents, and total surface currents, sampled in the cross-shore domain (a red box in Figure 1). The dominant variance of the geostrophic currents, which are estimated from the first spatial derivative of the SSH fields (equations 1 and 2), appear in the scales of longer than two days ($|\sigma| \le 0.5$ cpd) and larger than 25 km ($|k| \le 0.04\ \mathrm{km}^{-1}$) (Figure 2a). The differences between geostrophic currents and ageostrophic surface currents appear as the enhanced variance in the clockwise near-inertial and semi-diurnal (M_2) frequency bands and the reduced variance at low frequency ($|\sigma| < 0.4$ cpd) (Figures 2a and 2b). In particular, the influence of near-inertial motions and tidal currents on submesoscale scales can be significant. There is weak variance of the geostrophic currents in the near-inertial and semi-diurnal frequency bands, which can be considered as the estimation errors or signals (Figure 2a). Because the spatial derivatives of the (observed) high-resolution SSHs may have outliers in those frequency bands. In contrast, the currents estimated from finite differences of the TPXO barotropic model-derived tides (SSHs) at the K_1 and M_2 frequencies [TPXO version 7.2; [5]] using geostrophic balance ((equations 1 and 2) have the non-negligible amplitudes of approximately 6 $\mathrm{cm\,s}^{-1}$ and 1.2 $\mathrm{cm\,s}^{-1}$, respectively, and are visible in their energy spectra. Note that black boxes in Figures 2a to 2c indicate the temporal scale ($|\sigma| \le$ 0.5 cpd; $T \ge 2$ days) and spatial scale ($|k| \le 0.01\ \mathrm{km}^{-1}$; $\lambda \ge 100$ km) covered by [4], who focused on seasonal submesoscale processes owing to differences of seasonal mixed layers.

Similarly, the meridionally averaged rotary energy spectra of the currents are presented as a function of frequency and distance from the coast (Figures 3a to 3c). The variance of the geostrophic currents become dominant in the low-frequency band and its bandwidth becomes broadened near the coast ($0 < l \le 250$ km) (Figure 3a). In contrast, the ageostrophic surface currents contain variance in the near-inertial and low frequency bands and primary tidal frequencies (Figure 3b). Based on observations of surface near-inertial currents in the study domain, the enhanced variance of the offshore near-inertial currents decreases and disappears near the coast ($0 < l \le 30$ km) due to restricted circular inertial motions associated with the coastline and bottom topography. Similarly, the meridionally averaged rotary spectra of the AVISO geostrophic currents and HFR-derived surface currents (Figures 3d and 3e) are consistent with the variance distribution in the frequency and cross-shore direction even though they are only partially described in the temporal and spatial scales marked with black boxes in Figures 3a and 3c, respectively.

Retrieval of coastal submesoscale currents

A two-dimensional vector field can be described with vector components ($\mathbf{u} = [u\ \ v]^\dagger$, where † denotes the vector transpose) and a sum of vector components of velocity potential (ϕ) and stream function (ψ) using the Helmholtz decomposition:

$$\mathbf{u} = \mathbf{u}_\phi + \mathbf{u}_\psi = \nabla_h \phi + \mathbf{k} \times \nabla_h \psi. \qquad (5)$$

The concatenated matrix (ξ) of the velocity potential and stream function at the s-th regular grid point is estimated from multiple vector current data ($\mathbf{u} = [u\ \ v]^\dagger$) within a search radius from the grid point,

$$\hat{\boldsymbol{\xi}} = \mathrm{cov}_{\mathrm{dm}}^\dagger\, \mathrm{cov}_{\mathrm{dd}}^{-1}\mathbf{u}, \qquad (6)$$

where $\hat{\boldsymbol{\xi}} = [\hat{\phi}\ \ \hat{\psi}]^\dagger$ denotes the estimated velocity potential and stream function. Note that any assumptions are not required such that the two-dimensional vector field is either non-divergent or irrotational.

To identify the coherent frequency band between ψ and η, their coherence ($\hat{c}$) is presented as a function of distance from the coast.

$$\hat{c}(\mathbf{x},\sigma) = \frac{|\langle \hat{\psi}(\mathbf{x},\sigma)\, \hat{\eta}^\dagger(\mathbf{x},\sigma)\rangle|}{\sqrt{\langle|\hat{\psi}(\mathbf{x},\sigma)|^2\rangle}\sqrt{\langle|\hat{\eta}(\mathbf{x},\sigma)|^2\rangle}}, \qquad (7)$$

where $\hat{\psi}$, $\hat{\eta}$, $\langle\cdot\rangle$, and $\dagger$ denote the Fourier coefficients of stream function and SSH time series, the ensemble average, and the matrix transpose, respectively.

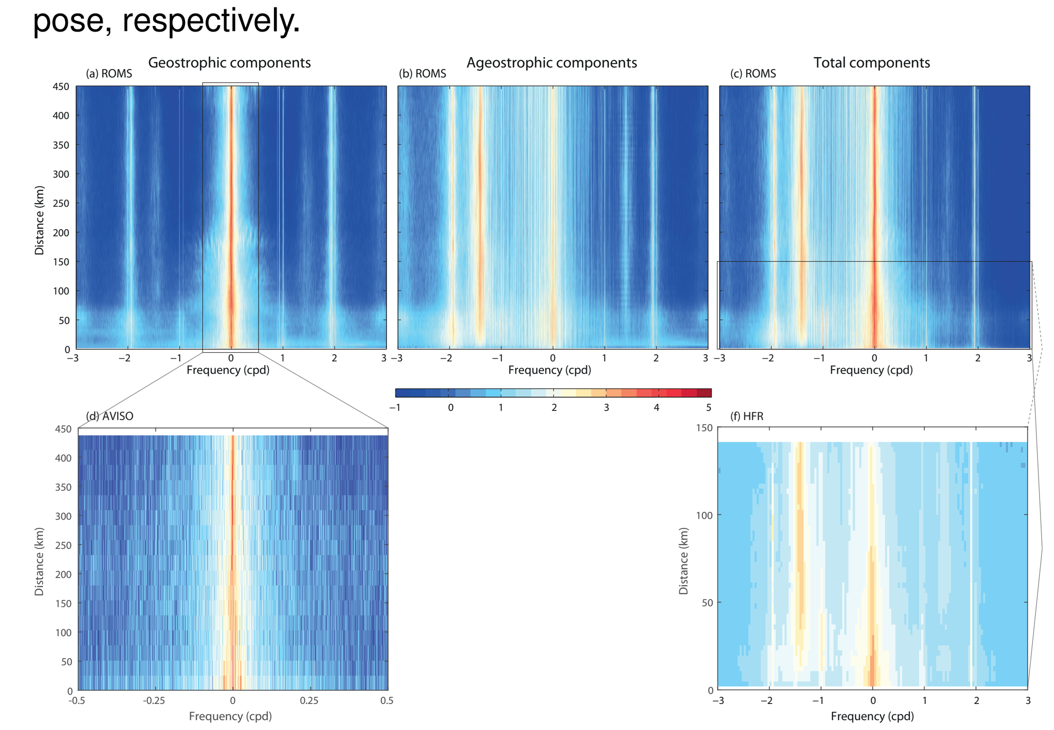

Figure 3: Meridionally averaged rotary energy spectra ($\log_{10}$ scale; $\mathrm{cm}^2\,\mathrm{s}^{-2}\,\mathrm{cpd}^{-1}$) of the (surface) currents derived from the numerical model simulation and observations. (a) ROMS-derived geostrophic currents. (b) ROMS-derived ageostrophic surface currents. (c) ROMS-derived total surface currents. (d) and (e): Observations. (d) AVISO geostrophic currents. (e) HFR-derived surface currents, which was modified from Figure 1d in [6]. Note that all currents are sampled within a latitudinal band (44°N and 45°N), (a) to (d) share the same colorbar, and the black boxes in Figures 3a and 3c correspond to the temporal and spatial scales in Figures 3d and 3e, respectively.

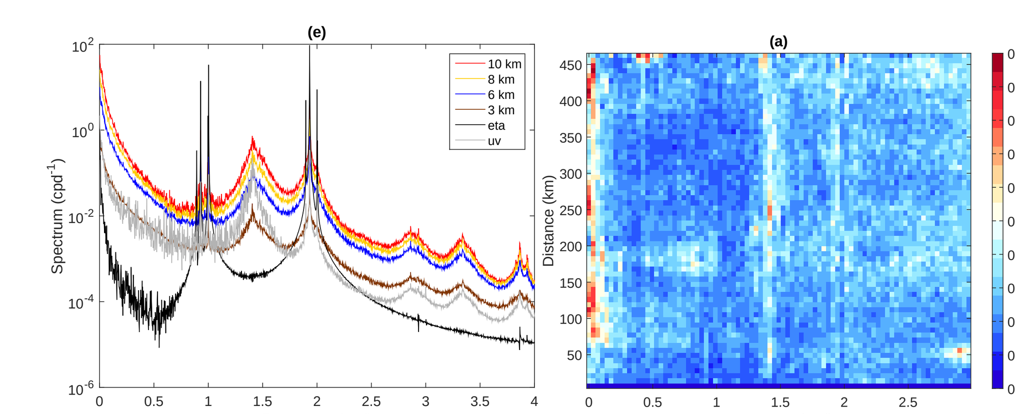

Figure 4: (a) Spectrum comparison of estimated ψ and η, and velocity components (u and v) at the 6 km resolution. (b) Averaged coherence between ψ and η as a function of distance and frequency.

Summary

We examined submesoscale ageostrophic coastal currents using numerical simulation output under realistic geophysical forcings and boundary conditions and compared with observations of high-frequency radar-derived surface currents and altimeter-derived geostrophic currents. The geostrophic currents are balanced currents between the Coriolis force and pressure gradients induced by spatial slopes in sea surface heights. The ageostrophic currents, i.e., the residual currents of the total currents with the geostrophic currents removed can be significant in coastal regions. In particular, submesoscale ageostrophic currents can be related to the vertical motions associated with internal waves and secondary circulations. Thus, their contribution to coastal circulations can be important. Based on forward regional circulation model outputs forced by wind stress and tides, the ageostrophic currents account for up to 50% of the total variance, and near-inertial variance contains approximately 40% of the variance of the ageostrophic currents.

Acknowledgement

This work is supported by a grant through Research for Applications of Geostationary Ocean Color Imager' through Korea Institute of Marine Science and Technology Promotion (KIMST), Ministry of Oceans and Fisheries, Republic of Korea. Special thanks to P. Michael Kosro and Alexander Kurapov at OSU for surface current data and numerical model outputs.

References

[1] S. Y. Kim, P. M. Kosro, and A. L. Kurapov. Evaluation of directly wind-coherent near-inertial surface currents off Oregon using a statistical parameterization and analytical and numerical models. *J. Geophys. Res.*, 119(10):6631 – 6654, 2014.

[2] JJ Osborne, AL Kurapov, GD Egbert, and PM Kosro. Spatial and temporal variability of the M_2 internal tide generation and propagation on the Oregon shelf. *J. Phys. Oceanogr.*, 41(11):2037–2062, 2011.

[3] A. E. Gill. *Atmosphere-Ocean Dynamics*, volume 30 of *International Geophysics Series*. Academic Press, 1982.

[4] Hideharu Sasaki, Patrice Klein, Bo Qiu, and Yoshikazu Sasai. Impact of oceanic-scale interactions on the seasonal modulation of ocean dynamics by the atmosphere. *Nature Commun.*, 5:1–8, 2014.

[5] G.D. Egbert, A.F. Bennett, and M.G.G. Foreman. TOPEX/POSEIDON tides estimated using a global inverse model. *J. Geophys. Res.*, 99(C12):24821 – 24852, 1994.

[6] S. Y. Kim, E. J. Terrill, B. D. Cornuelle, B. Jones, L. Washburn, M. A. Moline, J. D. Paduan, N. Garfield, J. L. Largier, G. Crawford, and P. M. Kosro. Mapping the U.S. West Coast surface circulation: A multiyear analysis of high-frequency radar observations. *J. Geophys. Res.*, 116, 2011.